JOURNAL OF SPACECRAFT AND ROCKETS
Vol. 39, No. 3, May–June 2002

Hypersonic Flow over a Blunt Body with Plasma Injection

J. S. Shang* and J. Hayes†
U.S. Air Force Research Laboratory, Wright–Patterson Air Force Base, Ohio 45433-7913
and
J. Menart‡
Wright State University, Dayton, Ohio 45435

The drag reduction of blunt body in hypersonic flow via plasma injection has been investigated by a combined experimental and computational effort. The counterflow plasma jet generated by a plasma torch has a vibrionic temperature of 4400 K, an electronic temperature around 20,000 K, and electron density greater than $3 \times 10^{12}/\text{cm}^3$. At a fixed injection stagnation pressure and in the absence of an applied magnetic field, the plasma injection actually increases drag above that of room-temperature air due to a decreased mass flow rate at the elevated temperature. However, at an identical mass flow rate, the plasma injection reveals a greater drag reduction than the room-temperature air counterpart through thermal energy deposition. From experimental measurements, an overwhelming major portion of the drag reduction is derived from the viscous–inviscid interaction of the counterflow jet and thermal energy deposition. The numerical results of Navier–Stokes equations with a local equilibrium plasma composition also confirm this observation.

Nomenclature

B = magnetic flux density, Wb/m^2
D = total drag
J = electrical current density, A/m^2
p = pressure, N/m^2 (Pa)
R = hemispherical nose radius, 3.81 cm
S = interaction parameter, $\sigma B^2 R/\rho u$
$\boldsymbol{U}$ = velocity vector u, v, w, m/s
Δ = standoff distance of bow shock
ρ = density, kg/m^3
σ = electrical conductivity, Ω^{-1}

I. Introduction

COUNTERFLOW jet interaction, electromagnetic forces, and nonequilibrium thermodynamics were speculated to be the key contributing mechanisms for supersonic aerodynamic drag reduction via plasma injection. In recent research efforts, a large amount of wave drag reduction is shown as the consequence of the counterflow jet and bow shock wave interaction.[1–3] The drag reduction from aerodynamic interaction is realized from altering a single bow shock to a multiple-shock structure by the counterflow jet. The contribution of nonequilibrium thermodynamics to drag reduction associated with plasma injection has been found to be insignificant.[4,5] For the drag reducing plasma injection phenomenon, the remaining uncertainty now resides in the relative magnitude of the aerodynamic and electromagnetic mechanisms. Thus, it is the main focus of the present investigation.

There is a great deal of work on the counterflow jet or the air-spike phenomena in the literature.[6–11] The counterflow jet or the jet spike of a blunt body in supersonic regime has two distinct states.[9–11] At the lower injection pressure, the jet displaces the bow shock upstream. The modified shock envelope is generally conical, and the flowfield is unsteady. At higher injection pressures, the displaced shock actually retracts back from the conical to a blunt configuration and returns to steady state.[1] The interaction of the counterflow jet with the bow shock is rather complex. The basic driving mechanism is the counterflow jet expanding into a low stagnation pressure bow shock envelope, then stagnating in the shock layer by a Mach disk. In essence, the flowfield consists of the counterflow jet issuing from the stagnation point and reversing its direction downstream as a free shear layer. A part of the jet stream is entrained to form a toroidal recirculation zone beneath the free shear layer. As the free shear layer reattaches to the blunt body, it induces a series of compression waves coalescing into a reattchment ring shock. The counterflow jet interaction replaces the single bow shock over a blunt body by a triple-shock structure.

The shock bifurcation phenomenon was discovered by the experimental study of the jet spike.[1,2] At the bifurcation point between steady and unsteady states, the drag reduction also attains the maximum value. The bifurcation is the consequence of breakdown of the subsonic feedback loop between the Mach disk and the unstable free shear layer.[1,12] As the jet injection rate increases, the subsonic region connecting the Mach disk and the free shear layer diminishes in size. At the bifurcation point, a portion of the counterflow, supersonic jet diverts from the Mach disk and effectively cuts off the upstream signal propagation from the free shear layer, and the oscillatory motion ceases.[1]

The controlling parameters of the counterflow jet are the jet mass flow rate, the jet exit Mach number, and the thermodynamic property of the injectant.[10] In the present effort, the jet exit Mach number is limited by a nozzle designed to accommodate a plasma torch. For plasma injection, the nonequilibrium weakly ionized air not only changes the temperature but also the thermodynamic property of the injectant. At present, an accurate description of the plasma is far from certain, but reasonable measurements of injectant temperatures are possible by emission spectra. Therefore, the thermal effect to plasma injection rate can be isolated and analyzed by solving the mass-averaged Navier–Stokes equations.

The electromagnetic force of the plasma injection may enter the interaction mostly through conductive current and transport of excess charges.[13] Significant charge separation may occur at locations where the disparity of electron and ion mobility are accentuated, such as near the electrodes and across the shock wave. Because an electromagnetic field modifies Rankine–Hugoniot condition across a shock (see Refs. 13 and 14), the charge separation at the shock wave is one of the likely sources to affect the wave drag. The joule heating and the work done by the Lorentz force on gas particles have also been demonstrated to be additional entropy alteration mechanisms.[1,2] However, note that, if the plasma maintains

Received 2 February 2001; revision received 29 August 2001; accepted for publication 1 November 2001.

*Senior Scientist, Center of Excellence for Computing Simulation; currently Research Professor, Department of Mechanical and Materials Engineering, Wright State University, 3640 Colonel Glenn Highway, Dayton, OH 45435-0001. Fellow AIAA.
†Aerospace Engineer, Center of Excellence for Computing Simulation.
‡Assistant Professor, Mechanical and Materials Engineering Department.

its global neutrality, a magnetic field must be applied to induce the electromagnetic and aerodynamic interaction. To further enhance the electromagnetic force in the present research, a magnetic field is also applied to increase the magnetic interaction parameter, $S = \sigma B^2 r/\rho u$ (Ref. 15). To quantify this interaction parameter, the electric conductivity of the plasma is measured by a double langmuir probe.

The present effort focuses on contributions of aerodynamic and possible electromagnetic forces to drag reduction via plasma injection at Mach 5.8. The theoretical work[13,14] has shown in a globally neutral plasma an applied magnetic field is the key for modifying the Rankine–Hugoniot condition. In the absence of an applied magnetic field, the electromagnetic contribution, if it exists, shall be very limited. A side-by-side experimental and computation effort is necessary to analyze the multidisciplinary problem. For computations, the mass-averaged, three-dimensional, Navier–Stokes equations are used to described the counterflow jet shock interaction and the high-temperature gas from the plasma.[16] The experimental research is conducted on a build-up approach; the counterflow jet is initiated by injecting air at room temperature and then ionized by a plasma torch in a single testing sequence. The drag variation during the testing sequence is recorded and analyzed. The experimental data include schlieren photographs, shock standoff distances with and without the ionized air, and the aerodynamic drag force measurement. The detailed flow structures within the displaced shock layer are analyzed by comparing experimental observations and numerical simulation.

II. Experimental Facility

The counterflow plasma jet and shock interaction is investigated in a blowdown, open-jet, high-Reynolds-number wind tunnel. This wind tunnel was designed to simulate flows at a nominal Mach number of 6.0, at the stagnation temperature of 610 K, and at a range of stagnation pressures from 3.44×10^2 to 1.40×10^4 kPa. The mass flow rate of the experiment spans a range from 0.77 to 4.63 kg/s, and the facility still can sustain a test period for up to 10 min. The force measuring model is a hemispherical cylinder, which has a nose radius and a total length of 38.1 and 203.2 mm, respectively. The counterflow jet aligns with the axis of the model and issues from the stagnation point. The ionized air of the jet is generated by a plasma torch embedded within the model. The aerodynamic force is measured by a set of three piezoelectric force sensors or load cells. Flowfield data are collected by an emission spectrometer for gas temperature and a double langmuir probe for electron density and electron temperature.

The Mach 6 tunnel can simulate atmospheric flight up to an altitude of 42.7 km (140,000 ft) with a Reynolds number of 45,200/m (1.38×10^6/ft). The available test core of the blowdown jet at the stagnation pressure of 6.89×10^2 kPa has a nominal diameter of 203.2 mm. The Mach number distributions across the jet core were surveyed at different streamwise locations and stagnation pressures; the deduced maximum variation is less than 2% (Refs. 2 and 3). This variation is measured within the domain bounded from the nozzle exit plane to a distance of 127 mm downstream. In addition, the axial flow gradient is negligible, and the operating Mach number of this tunnel is determined to be 5.80.

For the present investigation, the tunnel is operated at the lowest density of 0.0118 kg/m^3, which requires a mass flow rate of 0.77 kg/s at the freestream pressure of 2 torr. To circumvent the condensation of the air at the nozzle exit condition, the stagnation temperature is maintained at a constant value of 610 K and the static temperature of 79 K for all cases studied.

The model blockage interference in the wind tunnel has also been assessed by schlieren of bow shock waves around the model at the four survey locations.[3] The model is mounted on a retractable stem support in the testing chamber. The flowfield of the test section was also monitored by a static pressure gauge. No discernible blockage interference was detected. As an additional assurance, the standoff distance measured from the schlieren photograph ($\Delta/R = 0.157$) agrees with correlated data ($\Delta/R = 0.153$) by Ambrosio and Wortman.[17]

The model was fitted with three nozzles to calibrate the force measurements. The original design had a throat diameter D_t of 2.44 mm, and the exit Mach number was 2.86. At the same stagnation pressure as the tunnel running condition (344.7 kPa) but a lower stagnation temperature of 294 K, the calculated mass flow rate is 0.0038 kg/s (0.0084 lbm/s). The data collected from this nozzle essentially duplicated the previous measurements.[1,2] The second nozzle has a smaller throat diameter of 1.5 mm to accommodate the plasma torch. At the identical stagnation condition, the mass flow rate is 0.0014 kg/s (0.0032 lbm/s) and has an exit Mach number of 3.28. However, this mass flow rate is still too high for the torch to sustain the plasma generation. A third nozzle was designed with the throat diameter further reduced to 1.27 mm. This nozzle operated in the same stagnation condition as the others and the exit Mach number is 3.63 and yields the mass flow of 0.0010 kg/s. This nozzle flow changed from overexpanded to underexpanded condition at the stagnation pressure of 1077 kPa (156.24 psi).

III. Plasma Torch and Diagnostics

A plasma cutting torch from Thermadyne supplies the ionized air for the counterflow jet. This torch consists of two basic units: the PAK Master 50XL power supply and the PCH/M-28 torch. The maximum power output from this plasma torch is rated at 35 A with an ac input single-phase voltage of 208. However, in the present application, the unit is strictly operating in the starting mode. Therefore, the power output is far below the rated value. The arc starting circuit has a high-frequency generator that produces an ac voltage from 5000 to 10,000 V at a frequency of approximately of 2 MHz. The pilot arc within the torch head is maintained in the gap between the cathode and the positively charged tip. The pilot arc ionizes the compressed air passing through the torch head and exits through a small orifice in the torch tip with a swirling velocity component. The plasma is further expanded by a conical nozzle built in the force measuring model. As already mentioned, the nozzle has a throat diameter of 1.27 mm, an exit diameter of 3.53 mm, and an overall length of 8.13 mm. The plasma jet exits the nozzle at a Mach number of 3.64 if a sonic condition prevails at its throat.

Initially the rotational temperature of air plasma is attempted by the optical emission from the second positive electronic transition

$$C^3\Pi_u \rightleftharpoons B^3\Pi_g$$

of molecular nitrogen.[18–20] Unfortunately, the nitrogen C–B spectra were obscured by emission from other species, such as molecular oxygen and nitric oxide, as well as vapors of copper and iron. However, the origin band (0,0) of the ionized nitrogen N_2^+,

$$C^2\Pi_u^+ \rightleftharpoons X^2\Pi_g^+$$

appears as a prominent feature in the plasma torch emission spectrum. A composite spectrum of the plasma torch in the 3400–4400-Å wavelength range was obtainable.[19,20] The vibrionic temperature, determined from the Boltzmann plot, and a blackbody modeling is 4400 ± 400 K.

The electron density and temperature of the plasma field around the torch is measured by a double langmuir probe.[21,22] The probe is constructed from 0.5-mm platinum wire. The electrical potential is provided by a ± 100 V Keppco bipolar power supply. To determine the entire current–voltage characteristic, electrical current measurement capability in microamperes range is essential. For that purpose, the resistor in the circuit can vary from 75 to 1000 Ω (Ref. 22). The langmuir probe has a double-hole ceramic sleeve and a wire separation distance of 3.2 mm, and the sensing area of each probe is 3.9 mm^2. Although the platinum wire has a high resistance to oxidation at high temperature, the langmuir probe is still limited to the fringe area of the plasma torch. Preliminary data indicate that the electron density within the shock layer is 3×10^{12}/cm^3.

Once all of the transport properties of the weakly ionized gas are known, the drag modified by the plasma jet can be quantified in terms of the interaction parameter $S = \sigma B^2 R/\rho u$. The force measuring model is isolated from the support strut by a set of three load cells to receive the axial force exerted on the model. These load cells, or quartz-force rings (ICP Model 201B03), have a maximum compression range of 11.1 kN and a sensitivity of 44.4 N. The force data are recorded by these cells by a prestressed load of 2.2 kN to operate

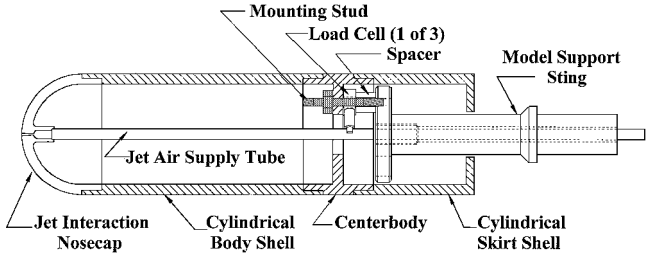

Fig. 1 Force measuring model.

in the linear measuring range. By this arrangement, the total force from the wave drag, skin-friction drag, and base drag is measured. The model design and fabrication is provided by K. Chadwick of the Massachusetts Institute of Technology Lincoln Laboratory. This model is shown in Fig. 1.

To differentiate the electromagnetic effect from the aerodynamic interaction and thermal phenomenon, an applied magnetic field is also imposed on the plasma stream. A set of neodymium rare earth (NeFeB) magnet collars have also been placed around the counterflow nozzle, and the maximum magnetic flux density at the pole registers a value of 0.47 T. The polarity of these magnets is aligned to the axis of the nozzle. Thus, the magnetic field is expected to show some influence on the swirling component of the plasma stream that issues from the torch head. In particular, the magnetic field may modify the drift motion of charged particles and especially the movement of electrons.

For experiments, the key difficulties are in the determination of the plasma transport properties discussed earlier. The experimental data are limited to nonintrusive, global measurements to yield a description from observations. At the plasma temperature around 4400 K (7260°R) and static pressure within the shock layer of 10.5 kPa (78.9 torr), the plasma chemical composition in equilibrium condition can be determined from numerous databases.[23] In terms of mass fraction, the components of N^+, NO^+, N_2^+, and O^+ are in the order of magnitude from 10^{-10} to 10^{-5}. In the state of the art for modeling hypersonic flow physics, the nonequilibrium thermodynamic state and internal energy partition can not be predicted with a desired degree of assurance.[24–26] For an example, the dissociation rates at high temperatures differ by more than a factor of 10 (Ref. 25). In standoff distance predictions for a nitrogen flow, two well-established rational vibrational relaxation models have yielded a discrepancy of 8% (Ref. 26). To avoid this uncertainty, the fluid dynamic behavior of the aerodynamic interaction is evaluated by the mass-averaged, time-dependent, three-dimensional, Navier–Stokes equations without the nonequilibrium chemical kinetics consideration.

IV. Numerical Analysis

All numerical results are generated by an implicit, unstructured Euler/Navier–Stokes equations solver, Cobalt.[16] The basic algorithm is that of Godunov's Riemann formulation (see Ref. 27) coupled with implicit time stepping to yield second-order spatial and temporal accuracy. The procedure is developed for a cell-centered, finite volume approach and is able to accommodate a single grid system, which may consist of a variety of cell types, tetrahedron and hexahedron in three-dimensional space. The governing equations are discretized by the fully implicit numerical scheme as

$$[3(\boldsymbol{U}^{n+1} - \boldsymbol{U}^{n}) - (\boldsymbol{U}^{n} - \boldsymbol{U}^{n-1})]/2\Delta t + \nabla \cdot \boldsymbol{F} = 0 \qquad (1)$$

where the $\boldsymbol{U}$ are the conservative independent variables $\boldsymbol{U}(\rho, \rho u, \rho v, \rho w, p)$ and $\boldsymbol{F}$ are the flux vectors of the Navier–Stokes equations. The reconstruction of the flux vectors at the centroid of the cell faces is by a least-square solution to the following approximation[16]:

$$\boldsymbol{U}_{i \pm \frac{1}{2}} = \boldsymbol{U}_i \pm \bar{r} \cdot \nabla \boldsymbol{U}_i \qquad (2)$$

where $\boldsymbol{U}_{i \pm 1/2}$ are the reconstructed left and right side of the variables at the cell interface and $\Delta \boldsymbol{U}_i$ is the gradient vector for the cell i.

An ingenious limiter of Cobalt has enhanced the unstructured grid procedure to control effectively the numerical dissipation for solving problems even with poor grid topologies. Another outstanding feature of Cobalt is the high parallel computing efficiency. The neighbor-cell connectivity of a unstructured grid formulation exhibits an exceptionally scalable, parallel computing performance on all multicomputers using a message passing interface (MPI) library.[28]

In the present application, the no-slip velocity components and adiabatic temperature conditions are imposed on the blunt-body surface. For the plasma torch, the sonic throat is designated at the entrance boundary for the conical injecting nozzles. The unperturbed freestream condition is specified at the upstream boundary and the no-reflection condition downstream for the far field. Turbulent closure is achieved by the Spalart–Allmaras one-equation model.[29]

V. Accuracy Assessment

The uncertainty in experimental data arise from the drag measurement using load cells. These piezoelectric quartz sensors have built in microelectronic amplifiers, which convert the high-impedance electrostatic charge from the crystals into a low-impedance voltage output. Therefore, it is most effective for measuring in a dynamic event. In the present investigation, the testing sequence is designed to take advantage of this feature. In that, the model is injected into the open jet of the tunnel, starts the counterjet from an air supply at room temperature (294 K), and then ignites the plasma for a fixed duration. Efforts have been devoted to maintain an isolated environment for the sensors from electromagnetic and thermal interferences. From this consistent calibration process, the data scattering band is repeatable by a data collection sweep over a period of 30 s.

In Fig. 2, individual data sweeps of three different counterflow nozzle configurations are presented. These data were collected at the lowest static pressure running condition of the tunnel, 2 torr. The tunnel operating condition is maintained by the stagnation temperature and pressure of 610 K and 344.7 kPa, respectively. The nozzle fitted with the plasma torch exhibited different performance characteristics when the supply air is routed through the plasma torch head. The air streaming through the plasma torch has a swirling velocity component for electrode cooling. Therefore, it is the most important baseline data.

The shock bifurcation phenomenon associated with the counterflow jet is clearly revealed in the drag measurements.[1] At the low injection stagnation pressure region, the drag is monotonically decreased until a critical point of injecting pressure. In this pressure range, the shock waves are unsteady until the injection pressure exceeds the critical value. Then the flowfield returns to steady state. The bifurcation controlling mechanism is the feedback loop connecting the free shear layer and the jet-forward-motion-terminating Mach disk.[1,2] For the $D_t = 2.23$, 1.50, and 1.27 mm nozzles, the critical values of P_j/P_0 at the bifurcation point are 1.0, 1.5, and 3.5, respectively. The much lower mass flow rate of the $D_t = 1.27$ mm nozzle has limited the plasma injection experiment exclusively in the unsteady flow region. From this set of data, the indicated scattering

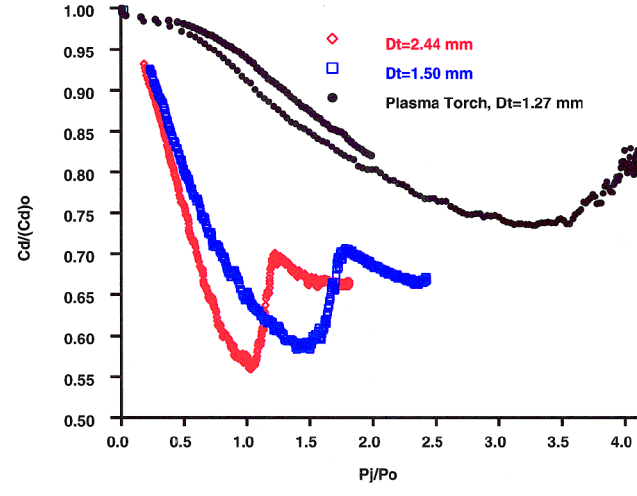

Fig. 2 Drag data of counterflow jet interaction.

band is less than 1.7%. However, the major portion of the data discrepancy between sweeps is in the determination of the absolute drag value after the model is injected in the tunnel jet stream. The measurement uncertainty is around 7%.

Another source of the uncertainty of the experimental data is the thermodynamic state and transport property of the plasma. The vibrionic temperature of the plasma is determined to be 4400 ± 400 K. It is arguable that the internal degrees of freedom of translation, rotation, and vibration are in thermal equilibrium.[18,19,24,25] The electron temperature deduced from a langmuir probe was measured to be 20,000 K. The corresponding electron density, which is highly dependent on the location relative to the plasma plume, yielded a value of $3 \times 10^{12}/\text{cm}^3$ or higher. An assessment of species concentration at the equilibrium state has been discussed earlier; it is assumed the chemical composition of the plasma torch is close to a state of thermal equilibrium for internal degrees of excitation up to dissociation. Therefore, the only distinct temperatures are that of electron and the heavy particles. This assumption is based on the observation that the density in the shock layer is sufficiently high to enhance high collision frequencies for energy transfer among internal energy modes.[24,25] Furthermore, the nonequilibrium chemical kinetic effects on the flow may be small in view of the relatively low temperature of the gas mixture and the even lower mass fraction of air components in ionized mode.[4,5,26]

The numerical error of any computing simulation consists of two elements: inappropriate governing equations and computational accuracy.[30] Because the error that incurred by solving overly simplified governing equations for magnetoaerodynamic phenomena presently cannot be assessed, neither the finite-rate chemical kinetics nor the finite electrical conductivity electromagnetic effects have been taken into consideration for numerical analysis. The computational accuracy is assessed by grid refinement studies of the three-dimensional mass-averaged, Navier–Stokes equations. Therefore, the effect of counterflow jet shock interaction can be accurately simulated. The effect of chemical kinetics to drag reduction is estimated on the measured vibrionic and electron temperatures. Finally the electromagnetic effect must rely on the experimental measurement. The present approach, reflects the state-of-the-art development in this scientific discipline.[31]

For a shock dominant problem, the criterion of numerical error evaluation is the shock definition and its standoff distance. In essence, the captured shock region is only first-order accurate for all approximate Riemann formulations.[27] The computational error is assessed by generating solutions on consecutively refined grids immediately adjacent to the shock. For an embedded conical nozzle in the hemispherical cylinder with a throat diameter of 2.44 mm and exit diameter of 4.70 mm, the exit Mach number is 2.86. Numerical solutions at a freestream Mach number of 5.80 on three grid systems of 185,484, 256,824, and 303,804 were obtained. The grid refinement was focused on the anticipated bow shock location. The calculated shock standoff distances, defined by the sonic point of the captured shock, were essentially grid independent after the first grid refinement.[1,2] The identical process was also applied to nozzle configurations of smaller throat diameter nozzles ($D_t =$ 1.27 mm).

The validating drag computations over the entire counterflow jet stagnation pressure range from 0 to 550.4 kPa are shown in Fig. 3. The corresponding data were collected at the lowest tunnel static pressure of 2 torr. The calculated result includes the base drag correction from experimental measurements. The base drag evaluated from two pressure taps in the model base region yields a constant value of 2.32 N over the entire tested range. An overall reasonable agreement is achieved for the strong aerodynamic interaction, including the bifurcation point. The maximum disparity between data and computations appears in the critical point of shock bifurcation, the numerical result underpredicts critical pressure ratio by about 10%. The calculated drag reduction is also persistently lower than data by 5%.

VI. Thermal Effect of Counterflow Jet

The counterflow jet in supersonic stream has been investigated since the 1960s.[6–11] The aerodynamic phenomenon evolves around

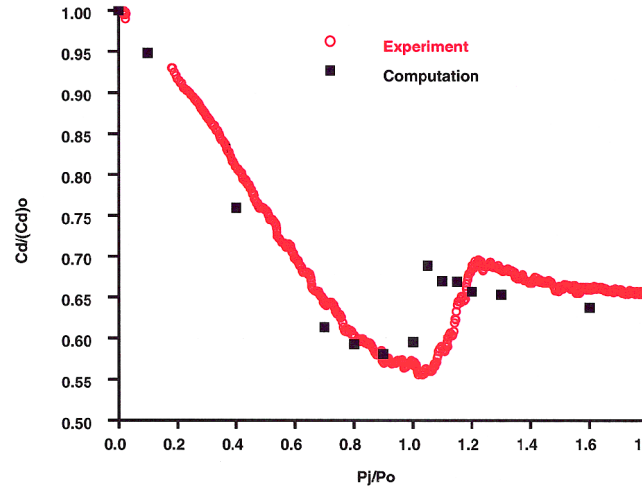

Fig. 3 Comparison of computed and measured drag.

the interaction of the counterflow jet and the bow shock. Initiating the counterflow jet into the shock layer does not require a high stagnation pressure because of the overwhelming stagnation pressure loss across the bow shock. The stagnation pressure in the shock layer of the present test is 11.84 kPa. As the injecting pressure of the counterflow jet increases, the jet changes from an overexpanded to an underexpanded state.[6–8] The overexpanded jet separates from nozzle wall and induces a very complex flowfield structure in the nozzle. However, influence of the separated flow within the nozzle to the overall flowfield is limited. On the other hand, the underexpanded jet can penetrate deeply into the shock layer. The resulting strong interaction consists of the counterflow jet, a forward-motion-terminating Mach disk, the reversing free shear layer over the toroidal recirculating zone, and a reattaching ring shock. This complex multiple shock structure leads to a substantial wave drag reduction. However, the most interesting phenomenon is the shock wave bifurcation, which has been discussed earlier.[1,2]

According to Barber,[10] the Mach number of the counterflow jet, mass flow rate, and chemical composition of the jet are important parameters in studying this phenomenon. However, the aerodynamic interaction is too complex to establish a usable correlation through a parametric study. For example, the effect of nonequilibrium chemical kinetics of sparse populated electrons in a relatively low gas temperature environment is difficult to estimate accurately.[24,25,31] In other words, the magnitude of these effects to drag reduction is so small and falls into error bands of numerical simulation. A similar argument equally applies to account for the electromagnetic effect in globally neutral plasma. In any event, experimental observations using an applied magnetic field to highlight the electromagnetic force through the plasma pinch effect are planned. For these reasons, the present effort must concentrate on the thermal effect of the plasma injection.

A series of computations of the counterjet issued from the conical nozzle with a throat diameter of 2.44 mm are recorded to duplicate the tunnel flow condition, $p_0 = 344$ kPa and $T_0 = 610$ K. The stagnation pressure of the jet is held at a constant value of 241.3 kPa for a range of stagnation temperatures from 294 to 4400 K. In Fig. 4, the calculated drag coefficients are compared with data and are seen to increase as the stagnation temperature of the injecting jet rises. In other words, the drag reduction by the counterflow jet diminishes when the temperature of the injectant is elevated, while the injecting stagnation pressure is held at a constant value. From the well-known performance characteristic of a nozzle, the lower injecting mass flow rate at the high stagnation temperature is the main source of drag variation.

Based on the present numerical results, the mass flow rate issuing from the jet decreases as the stagnation temperature increases. This behavior agrees with theoretical results for ideal nozzle flow in that the mass flow rate is linearly proportional to the stagnation pressure and inversely proportional to the square root of the nozzle stagnation temperature, $\dot{m} \sim (p_0/\sqrt{T_0})_j$. The comparison of the calculated

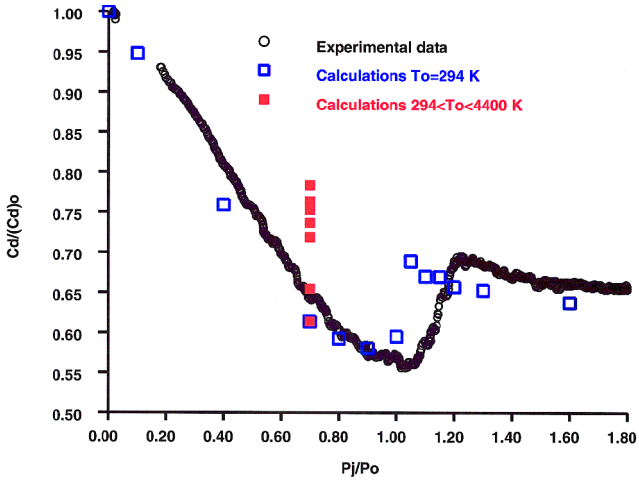

Fig. 4 Computed drag vs stagnation temperatures.

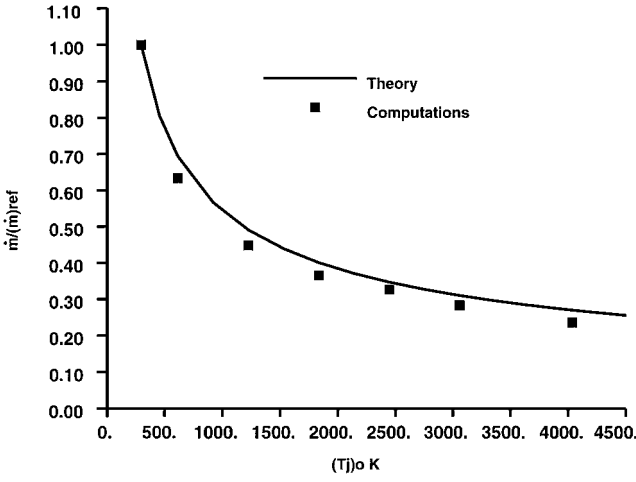

Fig. 5 Comparison of mass flow rates.

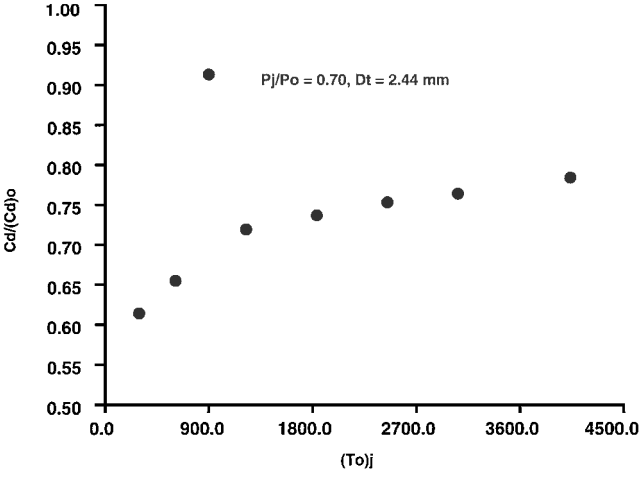

Fig. 6 Effect of nozzle stagnation temperature on calculated drag.

mass flow rate to theory is presented in Fig. 5. The maximum discrepancy between results is less than 8.5%. In the present analysis, a further breakdown of the sources of discrepancy from either the nonuniform velocity profile at the nozzle throat or the separated flow within the overexpanded nozzle is not possible. The computed mass flow rate of the counterflow jet decreases by a factor of 3.86 from the room-temperature to the plasma injection condition.

The computed drag at a constant injecting stagnation pressure (241.3 kPa) but increasing stagnation temperatures is shown in Fig. 6. All numerical results presented are obtained by solving the

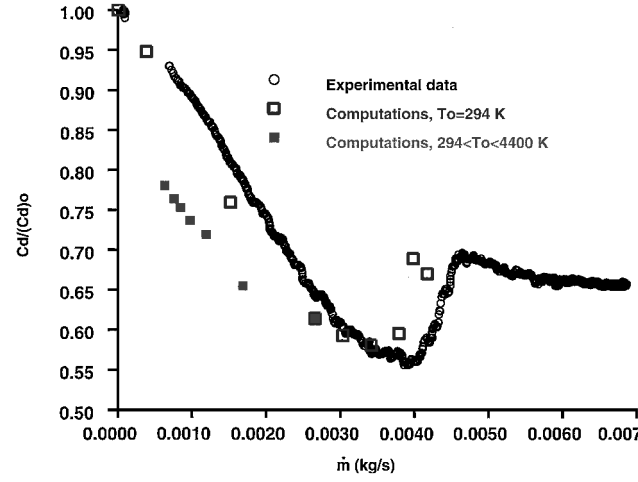

Fig. 7 Drag distribution vs injecting mass flow rate.

Navier–Stokes equations for perfect gas at the stagnation pressure of 344 kPa (50 psia) and a range of stagnation temperatures from 294 to 4040 K (530 to 7272 R). Although the mass flow rate is affected by the elevated stagnation temperatures, both theory and calculations show that the thrust from the nozzle remains unaltered. The reverse thrust is, thus, invariant with respect to the elevating stagnation temperature. Meanwhile, the counterflow jet with lower injecting mass flow rate has a reduced influence to modify the shock structure for wave drag reduction. As the consequence, the net drag of a blunt body with a counterflow jet increases with the rising stagnation temperature at a constant injecting stagnation pressure. As the stagnation temperature rises from 294 to 4040 K, the drag increases by a factor of 1.28 at a constant stagnation pressure.

The pure thermal effect of the counterflow jet on drag calculation is easily singled out by the present result as a function of the mass flow rate. In Fig. 7, the drag data and the computed results are presented together. The calculated drag coefficients at the same stagnation pressure, but different stagnation temperature, are presented as discrete points. The highest drag reduction of this series of calculations corresponds to stagnation temperature of the plasma. The anchor point of the specific comparison is the drag coefficient distribution at the stagnation temperature of 294 K. The calculated results indicate that, at a constant rate of mass flow, the higher stagnation temperature of the counterflow jet leads to a greater drag reduction. At the identical mass injection rate, the added thermal energy of the counterflow jet produces a monotonically increased drag reduction. The maximum additional drag reduction is 13.4% at the plasma temperature with a mass flow rate of 0.00063 kg/s.

The computed flowfields at a stagnation pressure of 243.3 kPa and stagnation temperatures of 294 and 4400 K are shown in Fig. 8. The latter case is intended to duplicate the thermal condition of the plasma torch with the perfect gas model. As noted, in all numerical simulations up to this point, the nonequilibrium excitations beyond the rotational degree of freedom are excluded. Nevertheless, the numerical results reveal that the higher temperature counterflow jet has a much shorter penetration depth in the shock layer than the lower temperature counterpart. This behavior is anticipated from a substantially reduced mass injection rate at the higher temperature. The thermal diffusion of the higher temperature can also dominant over the lower temperature injectant as expected. The lower density within the shock layer also forces a standoff distance adjustment at the intersection of the bow shock and the ring shock to accommodate the identical freestream. This outward displacement of the shock wave produces a more obtuse shape than the colder air injection.

Because the plasma temperature is a direct measurement from the optical emission of ionized nitrogen N_2^+,

$$C^2\Pi_u^+ \rightleftharpoons X^2\Pi_g^+$$

the partition of internal energy has already affected the temperatures of the gas mixture.[18,19,31] Although the detailed thermodynamic state

of the plasma is uncertain, the equilibrium composition of the plasma at the measured temperature can be accurately determined.[23] From the equilibrium chemical composition, additional computations using Navier–Stokes have been performed. In short, the calculated drag reductions based on equilibrium chemical composition are uniformly 3% less than that of the standard air calculations. These results reflect correctly that a part of thermal energy must be distributed to the higher degrees of freedom instead of converting into kinetic energy through the expansion process. In this sense, the present numerical results represent an ideal baseline for the thermal deposition of the counterflow jet.

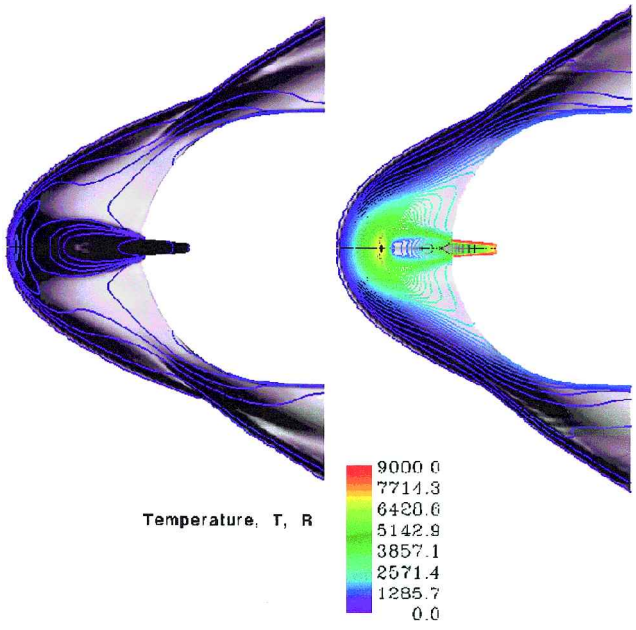

Fig. 8 Flowfield structures at different stagnation temperatures.

VII. Plasma Counterflow Jet

It is reasonable to assume that the vibrionic temperature (4400 ± 400 K) is in thermal equilibrium with all other degrees of freedom but not necessarily with electronic excitation.[14] In fact, this conjecture has received partial support from langmuir probe measurements in the fringe of the plasma plume. The measured electronic temperature is 20,000 K. In essence, the heavy particles temperature of the injected plasma is comparable to that reported by Ganiev et al.,[32] Bityurin et al.,[33] and Malmuth et al.[11]

The equilibrium chemical composition of the plasma counterflow jet can be determined in terms of mass fraction at the thermodynamic state near the Mach disk in the shock layer (4400 K and 10.5 kPa). The mass fractions of molecular nitrogen and nitric oxide are 0.68 and 0.05, respectively. The oxygen molecules are nearly all dissociated to yield a mass fraction of atomic oxygen around 0.26. The components of N^+, NO^+, N_2^+, and O^+ are in the order of magnitude from 10^{-5} to 10^{-10} (Ref. 23). These low mass fractions are essentially considered to be trace elements. Although the plasma counterflow jet is understood to be in thermodynamically nonequilibrium state, the chemical composition and internal energy partition can not be predicted with certainty. Therefore, the mass flow rates of the plasma counterflow jet were calculated based on the equilibrium composition to yield the tested mass flow rates of 0.0013, 0.0019, 0.0023, and 0.0026 kg/s, which correspond to the nominal injection pressure ratios p_j/p_0 of 1.4, 2.0, 2.5, and 2.8, respectively.

A photograph of the plasma counterflow jet injection is given in Fig. 9. The stagnation pressure of the jet is 482.6 kPa, and the ratio of the stagnation pressures of the jet and the tunnel is 1.4. For the $D_t = 1.27$ mm nozzle, the injecting rate is 0.0013 kg/s based on the assumptions that the sonic condition prevails at the throat, and the chemical composition of the plasma is not drastically different from the equilibrium condition. The added complication of nozzle wall erosion by oxidation renders an accurate calculation of the mass flow rate difficult. Nevertheless, the envelope of the plasma plume in the photograph coincides with the schlieren photograph of the shock wave system. The plasma also propagates along the blunt-body surface and persists far downstream.

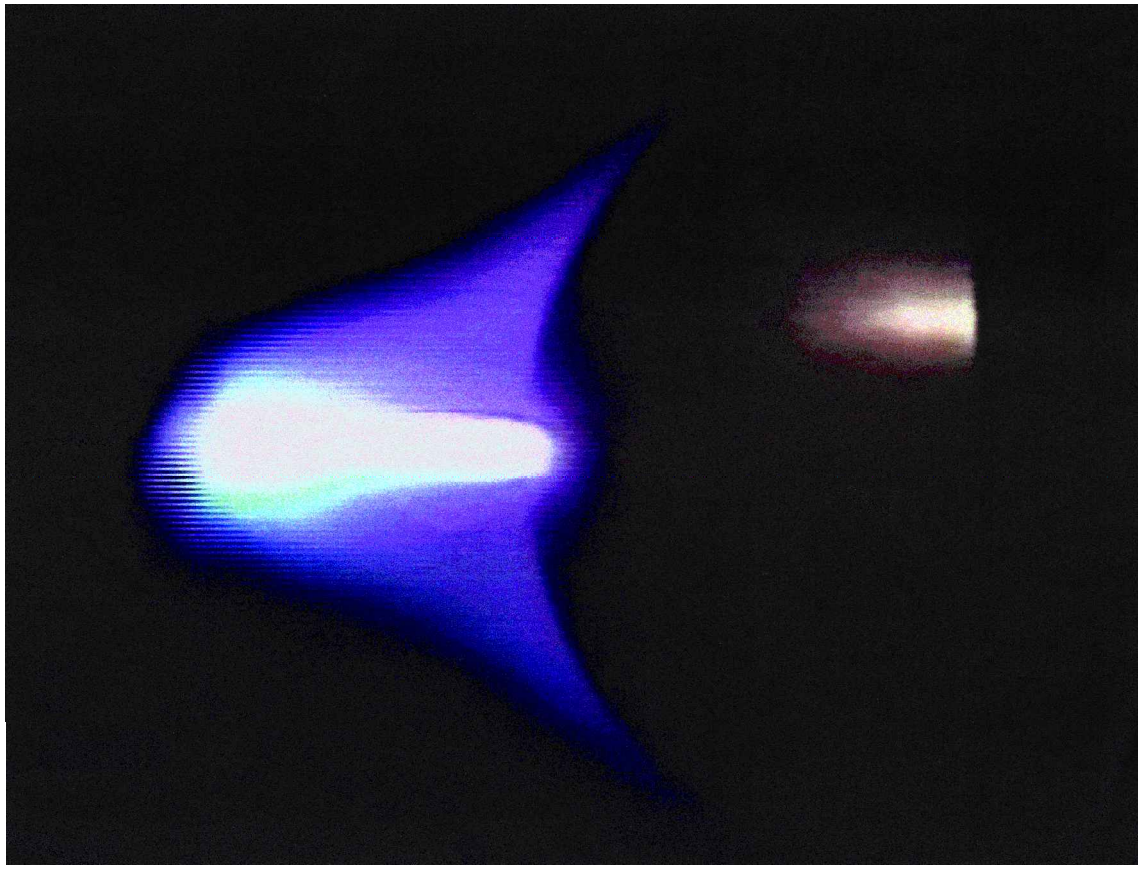

Fig. 9 Plasma counterflow jet and shock interaction.

The composite photograph of schlieren at four different stagnation pressures of the plasma counterflow jet is presented in Fig. 10. The plasma is injected into the bow shock envelope at stagnation pressures of 582, 689, 827, and 965 kPa (70, 100, 125, and 140 psia). Two major features of the plasma injection in contrast to the room-temperature jet stand out. First, the shock waves uniformly retract toward the blunt body for all cases tested. Based on the perfect gas model calculation, this phenomenon is mostly associated with a reduced mass flow rate by the elevated plasma temperature. Under the present testing condition, the mass flow rate is reduced by a factor of 3.7. However, the shock wave conformation is different from the typical lower mass injection.

The other feature of plasma injection is that the amplitude of the unsteady shock wave movement is significantly subdued. This behavior is dramatic on the video recording, and the same observation can also be made from the change from the relatively blurred photographic images of the room-temperature injection to the sharply defined shock structure by the plasma injection. At the lowest plasma injection pressure (482 kPa), two biased bow shocks appear to dominate over others, but the unsteady movement of shock waves persisted. These two contrasting features between the room-temperature air and plasma injection are uniformly observed over the entire tested pressure range.

The spectra information of drag measurements for the room-temperature air and plasma issued at the same stagnation pressure of 689 kPa (100 psia) are shown in Fig. 11. The sampled frequency covers a spectrum up to 5 kHz. The basic oscillatory behavior between two different injectant is similar, and the most predominant oscillatory mode occurs at 100 Hz. The amplitude of oscillations reduces significantly at the higher frequency. Over the frequency range from 500 to 2500 Hz, the oscillatory amplitude of the plasma injection is roughly 10 dB lower than the room-temperature air counterpart. The measured power spectral density fully supports the observation from the video records and schlieren photographs.

The plasma injection drag data ($D_t = 1.27$ mm nozzle) at four tested stagnation pressures of the plasma injection are presented in Fig. 12. The discrete data set is accompanied by results of

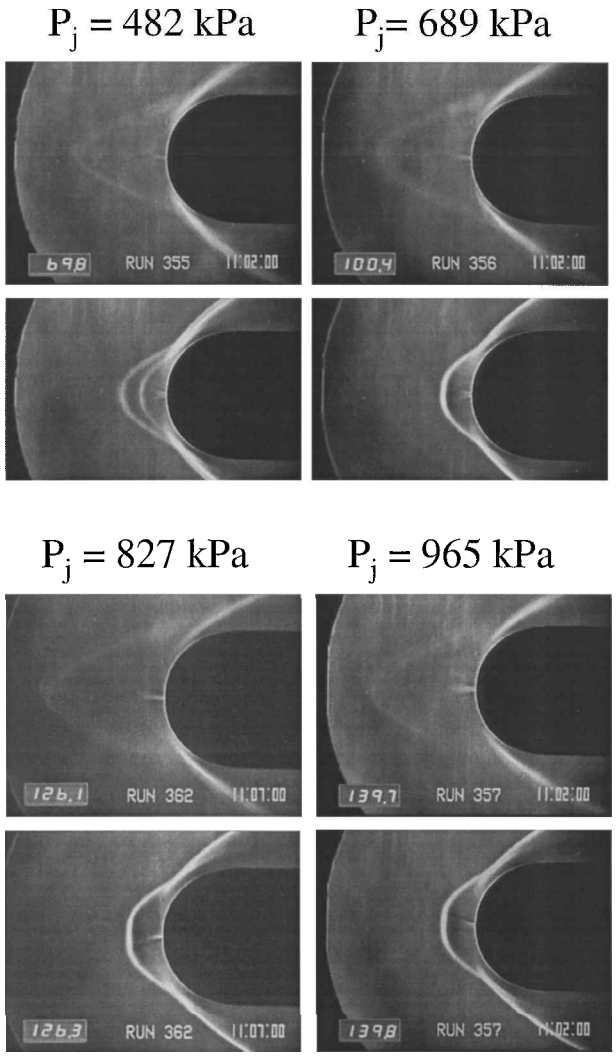

Fig. 10 Schlieren photographs of plasma injection.

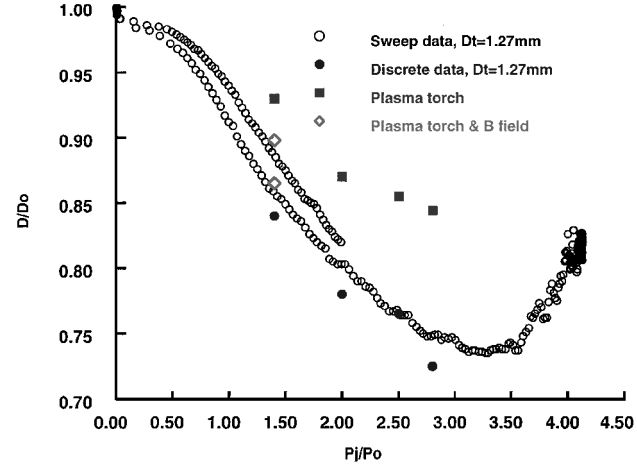

Fig. 12 Drag data of plasma injection vs P_j/P_0.

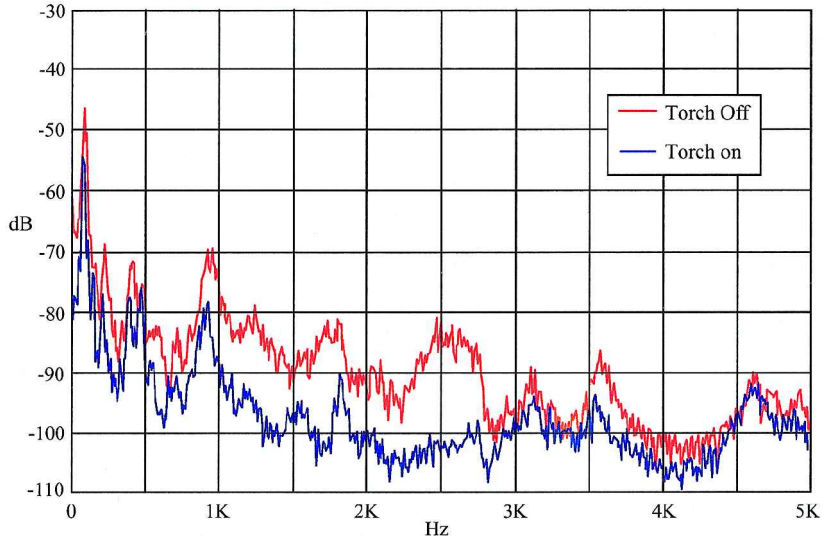

Fig. 11 Spectral density of drag measurement.

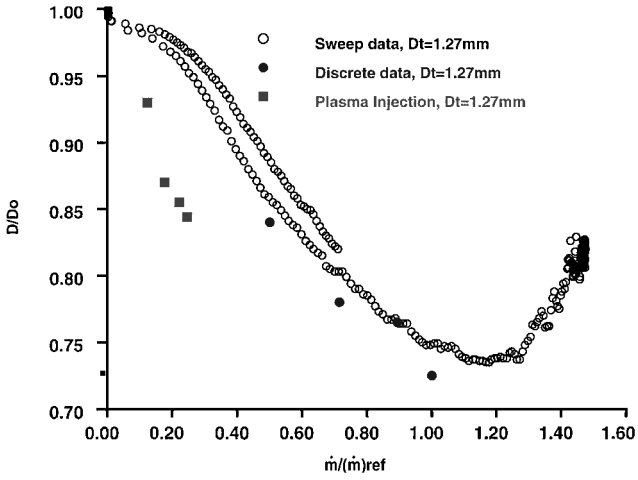

Fig. 13 Drag data of plasma injection vs $m/(m)_{ref}$.

room-temperature air injection in a single data sweep. This continuous data distribution serves as a reference for individual drag measurements. In the present data collection process, the drag measuring procedure starts with room-temperature air injection. The plasma is then introduced by igniting the torch, which is sustained for a duration of 15 s. In a typical test, the piezoelectric force sensors yield consistent output just a fraction of a second after the transient electromagnetic pulse has passed. The drag of an individual test by the room-temperature air injection registers a value close to the data of reference. The maximum difference is generally confined within the data scattering band of about 5%. The measured drags rise when the plasma is ignited. According to the earlier computational analyses of similar simulations, this behavior is mostly due to reduced mass injection flow rate. There is little doubt that the plasma injection has produced a greater drag reduction than the room-temperature air injection at the identical mass flow rate.

Identical experimental data are presented in terms of mass flow rate in Fig. 13. The mass flow rate is obtained by solving the mass-averaged Navier–Stokes equations using the the chemically equilibrium composition. The calculated mass flow rate yields values of 0.13, 0.19, 0.23, and 0.26 g/s, which correspond to the injecting stagnation pressure ratios P_j/P_0 of 1.4, 2.0, 2.5, and 2.8, respectively. The additional drag reduction by the thermal deposition of the plasma injection is clearly demonstrated. The computed magnitude of the reduced drag is as high as 13.4%.

In an attempt to further define the electromagnetic effect for the plasma counterflow jet, an applied magnetic field was imposed by a set of neodymium rare earth (NeFeB) magnets around the plasma torch chamber. The polarization of the applied magnetic field is aligned with the axis of the nozzle to enhance the plasma pinch effect.[21] The magnet has a maximum magnetic flux density of 0.47 T at the pole, but the field strength diminishes rapidly toward the nozzle axis. The estimated value is about 0.17 T locally, and the plasma interaction parameter $S(\sigma B^2 R/\rho u)$ is much less than unity. Under this circumstance, the effects of Lorentz force is difficult to detect. As anticipated, the only success was achieved at the lowest plasma stagnation pressure. The difference between plasma and room-temperature air injection including the applied magnetic field is detectable. The difference in drag measurement with and without an applied magnetic field is not consistent, but always less than 4%. The plasma also failed to ignite at all higher plasma stagnation pressures. Note that this magnetic field is applied only near the electrodes, where the electrical charge separation may take place. From this observation, one recognizes that the induced magnetic field by plasma injection is most likely negligible.[14,15,31] Therefore, a significant electromagnetic effect by plasma injection for flowfield modification would be highly doubtful.

From the present research results at an identical mass flow rate, the plasma injection indeed produces a greater drag reduction than its room-temperature counterpart. However, the major portion of the reduced drag of the present experiment is derived from the thermal deposition of the plasma. Another feature of the shock wave and plasma counterflow jet interaction lies in the unusual configuration of the complex shock waves. The resultant shock wave conformation at a lower mass flow rate does not follow the trend of the room-temperature air injection. The thermal diffusion can play a significant role in this phenomenon (see Fig. 8).

The charge separation across the bow shock leading to a steep electrical field gradient is another physical possibility. The mean free path of the oncoming stream under the tested condition is 3.35 μm (10^{-6} m), whereas the debye length of the plasma is about 11.0 μm. The debye length is, thus, more than a factor of three greater than the mean free path of the freestream, which is of the same order of magnitude of the shock wave thickness. As a point of reference, the electron mean free path is about 0.1 mm at the freestream pressure of 5 torr. This phenomenon remains as a key element for future investigation.

VIII. Conclusions

The drag reduction by a plasma counterflow jet is investigated in a Mach 6 wind tunnel at a freestream pressure of 344.7 kPa and temperature of 79 K. The plasma with a vibrionic temperature of 4400 ± 400 K, an electron temperature about 20,000 K, and an estimated electron density greater than $3 \times 10^{12}/\text{cm}^3$ is injected from a hemispherical cylinder. At a given stagnation pressure, the measured drag is nearly 10% higher than the room-temperature air injection. However, if the decreased injection mass flow by the elevated plasma temperature is taken into consideration, the drag reduction by plasma injection is in fact greater.

Based on the equilibrium chemical composition at the measured plasma condition and at the identical injecting mass flow rate, the plasma injection would yield a range from 6.1 to 13.4% greater drag reduction by the plasma thermal deposition. From the experimental data, the effects of chemical nonequilibrium and electromagnetic force are most likely negligible.

In addition to a greater drag reduction, the plasma injection reduces the amplitude of shock wave oscillation associated with the counterflow jet and bow shock interaction. In the injection pressure range lower than the shock bifurcation point, the plasma injection significantly reduces the oscillatory amplitude of drag measurements by 10 dB.

Acknowledgments

The computing resource was supported by a grant from the Department of Defense High Performance Computing Shared Resource Center at Wright–Patterson Air Force Base. The research team deeply appreciates the sponsorship by S. Walker of the Air Force Office of Scientific Research. The invaluable contributions by James M. Williamson, Dean Emmer, and the wind-tunnel crew, Tom Norris, Ray Raber, and Michael Greene are duly acknowledged.

References

[1]Shang, J. S., Hayes, J., Wurtzler, K., and Strang, W., "Jet-Spike Bifurcation in High-Speed Flows," *AIAA Journal*, Vol. 37, No. 6, 2001, pp. 1159–1165.

[2]Shang, J. S., Hayes, J., Harris, S., Umstattd, and Ganguly, B., "Experimental Simulation of Magneto-Aerodynamic Hypersonics," AIAA Paper 2000-2258, June 2000.

[3]Shang, J. S., Ganguly, B., Umstattd, R., Hayes, J., Arman, M., and Bletzinger, P., "Developing a Facility for Magneto-Aerodynamic Experiments," *Journal of Aircraft*, Vol. 17, No. 6, 2000, pp. 1065–1072.

[4]Josyula, E., "Computational Study of Vibrationally Relaxing Gas Past Blunt Body in Hypersonic Flow," *Journal of Thermophysics and Heat Transfer*, Vol. 14, No. 1, 2000, pp. 18–26.

[5]Wegner, P. P., and Buzyna, G., "Experiments on Shock Standoff Distance in Non-Equilibrium Flow," *Journal of Fluid Mechanics*, Vol. 32, Pt. 2, 1969, pp. 325–335.

[6]Adamson, T. C., and Nicholls, J. A., "On the Structure of Jet from Highly Under Expanded Nozzles into Still Air," *Journal of the Aeronautical Sciences*, Vol. 26, Jan. 1959, pp. 16–21.

[7]Warren, C. H. E., "An Experimental Investigation of the Effect of Ejecting a Coolant Gas at the Nose of a Bluff Body," *Journal of Fluid Mechanics*, Vol. 8, 1960, p. 400.

[8]Baron, J. R., and Alzner, E., "An Experimental Investigation of a Two Layer Inviscid Shock Cap Due to Blunt Body Nose Injection," *Journal of Fluid Mechanics*, Vol. 15, 1963, p. 442.

[9]Finley, P. J., "The Flow of a Jet from a Body Opposing a Supersonic Free Stream," *Journal of Fluid Mechanics*, Vol. 26, Pt. 2, 1966, pp. 337–368.

[10]Barber, E. A., Jr., "An Experimental Investigation of Stagnation-Point Injection," *Journal of Spacecraft and Rockets*, Vol. 2, No. 5, 1965, pp. 770–774.

[11]Malmuth, N. D., Fomin, V. M., Maslov, A. A., Fomichev, V. P., Shashkin, A. P., Korotaeva, T. A., Shipyuk, A. N., and Pozdnyakov, G. A., "Influence of a Counterflow Plasma Jet on Supersonic Blunt Body Pressures," AIAA Paper 99-4883, Nov. 1999.

[12]Rockwell, D., and Naudascher, E., "Self-Sustained Oscillations of Impinging Free Shear Layers," *Annual Review of Fluid Dynamics*, Vol. 11, 1979, pp. 67–94.

[13]Sutton, G. W., and Sherman, A., *Engineering Magnetohydrodynamics*, McGraw–Hill, New York, 1965, pp. 295–308.

[14]Mitchner, M., and Kruger, C. H., *Partially Ionized Gases*, Wiley, New York, 1973, pp. 163–241.

[15]Resler, E. L., and Sears, W. R., "The Prospects for Magneto-Aerodynamics," *Journal of the Aeronautical Sciences*, Vol. 25, 1958, pp. 235–245, 258.

[16]Strang, W. Z., Tomaro, R. F., and Grismer, M., "The Defining Methods of Cobalt: A Parallel, Implicit, Unstructured Euler/Navier–Stokes Flow Solver," AIAA Paper 99-0786, Jan. 1999.

[17]Ambrosio, A., and Wortman, A., "Stagnation Point Shock Detachment Distance for Flow Around Spheres and Cylinder," *ARS Journal*, Vol. 32, No. 2, 1962, p. 281.

[18]Gilmore, F. R., Laher, R. R., and Espy, P. J., "Franck–Condon Factors, r-Centroids, Electronic Transition, Moments, and Einstein Coefficients for Many Nitrogen and Oxygen Band Systems," *Journal of Physical and Chemical Reference Data*, Vol. 21, No. 5, 1992, pp. 1005–1107.

[19]Herzberg, G., *Molecular Spectra and Molecular Structure. I. Spectra of Diatomic Molecules*, 2nd ed., Van Nostrand, New York, 1950, pp. 146–314.

[20]Huber, K. P., and Herzberg, G., *Molecular Spectra and Molecular Structure, Vol IV: Constants of Diatomic Molecules*, Van Nostrand Reinhold, New York, 1979.

[21]Howatson, A. M., *Gas Discharges*, 2nd ed., Pergamon, Oxford, 1975, pp. 168–190.

[22]Menart, J., Shang, J. S., and Hayes, J., "Development of a Langmuir Probe for Plasma Diagnostic Work in High Speed Flow," AIAA Paper 2001-2804, June 2001.

[23]McBride, B. J., and Gordon, S., "Computer Program for Calculation of Complex Chemical Equilibrium Compositions and Applications, II. User Manual and Program Description," NASA Reference Publ. 1331, June 1996.

[24]Park, C., "Assessment of Two-Temperature Kinetic Model for Ionizing Air," AIAA Paper 87-1574, June 1987.

[25]Oertel, H., Jr., "Oxygen Vibrational and Dissociation Behind Regular Reflected Shocks," *Journal of Fluid Mechanics*, Vol. 74, No. 3, 1976, pp. 477–495.

[26]Josyula, E., and Bailey, R. F., "Vibration–Dissociation Coupling Using Master Equations in Nonequilibrium Hypersonic Blunt Body Flow," *Journal of Thermophysics and Heat Transfer*, Vol. 15, No. 2, 2001, pp. 157–167.

[27]Tannehill, J. C., Anderson, D. A., and Fletcher, R. H., *Computational Fluid Mechanics and Heat Transfer*, 2nd ed., Taylor and Francis, Washington, DC, 1997, pp. 351–437.

[28]Grismer, M. J., Strang, W. Z., Tomaro, R. F., and Witzman, F. C., "Cobalt: A Parallel, Implicit, Unstructured Euler/Navier–Stokes Solver," *Advances in Engineering Software*, Vol. 29, No. 1, 1998, pp. 365–373.

[29]Spalart, P. R., and Allmaras, S. R., "A One-Equation Turbulent Model for Aerodynamic Flows," AIAA Paper 92-0439, Jan. 1992.

[30]Shang, J. S., "An Assessment of Technology for Aircraft Development," *Journal of Aircraft*, Vol. 32, No. 3, 1995, pp. 611–617.

[31]Shang, J. S., "Recent Research in Magneto-Aerodynamics," *Progress in Aerospace Science*, Vol. 37, No.1, 2001, pp. 1–27.

[32]Ganiev, Y. C., Gordeev, V. P., Krasilnikov, A. V., Lagutin, V. I., Otmennikov, V. N., and Panasenko A. V., "Aerodynamic Drag Reduction by Plasma and Hot-Gas Injection," *Journal of Thermophysics and Heat Transfer*, Vol. 14, No. 1, 2000, pp. 10–17.

[33]Bityurin, V. A., Velikodny, V. Y., Klimov, A. I., Leonov, S. B., and Potebnya, V. G., "Interaction of Shock Waves with a Pulse Electrical Discharge," AIAA Paper 99-3533, June 1999.

T. C. Lin
Associate Editor

Color reproductions courtesy of the U.S. Air Force Research Laboratory.